

Compressible Baker Maps and Their Inverses .

A Memoir for Francis Hayin Ree [1936-2020]

William Graham Hoover
Ruby Valley Research Institute
Highway Contract 60, Box 601
Ruby Valley, Nevada 89833
(Dated: December 25, 2020)

Abstract

This memoir is dedicated to the late Francis Hayin Ree, a formative influence shaping my work in statistical mechanics. Between 1963 and 1968 we collaborated on nine papers published in the Journal of Chemical Physics. Those dealt with the virial series, cell models, and computer simulation. All of them were directed toward understanding the statistical thermodynamics of simple model systems. Our last joint work is also the most cited, with over 1000 citations, “Melting Transition and Communal Entropy for Hard Spheres”, submitted 3 May 1968 and published that October. Here I summarize my own most recent work on compressible time-reversible two-dimensional maps. These simplest of model systems are amenable to computer simulation and are providing stimulating and surprising results.

Keywords: Francis Ree, Statistical Physics, Reversibility, Maps, Information and Kaplan-Yorke Dimensions

I. FRANCIS HAYIN REE [JULY 1936–JANUARY 2020]

In 1962 I was hired as a physicist (despite Master's and Doctor's degrees in physical chemistry) by the Lawrence Radiation Laboratory in Livermore, California. I had read that Berni Alder and Tom Wainwright were developing molecular dynamics there¹, working with hard disks and spheres, closely related to my parallel hard-square and hard-cube thesis work under Andy De Rocco at Ann Arbor^{2,3}. Francis Ree was already established at Livermore, on LRL's square mile. He was fresh from his own doctoral work, at the University of Utah under Henry Eyring, on random walks⁴. Both of us were happy to have access to Livermore's tremendous computational power, along with help from the Laboratory's hundreds of stimulating Ph Ds. Francis and I shared the computational services of Warren Cunningham. Warren kindly punched the cards and fetched the printouts, by Laboratory bicycle, as we explored the application of statistical mechanics to simple models, settling into lifelong regimens of research and publication.

II. NONEQUILIBRIUM SIMULATIONS *VERSUS* CARBON COMPOUNDS

From the hard-sphere equation of state and integral equations for few-body distribution functions Francis concocted general predictive recipes for pressure-volume-energy equations of state for air, water, hydrocarbons, and high explosives. His enthusiasm for phase transitions, honed on simple statistical models and the rare gases, carried over to carbon with its graphite and diamond phases. Francis generated accurate thermodynamic data for pentaerythritol tetranitrate, a high-explosive relative of nitroglycerine. He described the behavior of polybutene and phase-diagram behaviors of the rare gases, graphite and diamond, as well as many of carbon's compounds, both organic and inorganic⁵. He became a permanent member of the Korea Academy of Science and Technology. He received the Department of Energy's Award of Excellence and two Lawrence Livermore National Laboratory Distinguished Achievement Awards after contributing thirty years' work to the Livermore Laboratory. A scholar and a gentleman.

By 1970 Francis' and my research paths had separated. Berni Alder had helped me to a Professorship at the University of California's Department of Applied Science. There I worked with my first Ph D student, Bill Ashurst. We set out to develop nonequilibrium

atomistic solution techniques, “nonequilibrium molecular dynamics”⁶. Meanwhile Francis was drawn to more realistic representations of the relatively complex systems supporting the Livermore Laboratory’s weapons programs. He carried out over 100 research inquiries with dozens of coauthors. Most of his work had its base in relatively esoteric elaborations of equilibrium statistical mechanics. That underlying theory was applied to down-to-earth practical applications for materials relevant to weapons research.

Meanwhile my own work progressed along lines more academic than applied, facilitated by my joint appointments in the University and the Laboratory. Bill Ashurst and I mostly restricted our collaborative work to the Lennard-Jones pair potential, a crude representation of argon, developing simulations of its equilibrium and nonequilibrium properties (viscosity and thermal conductivity). In inventing nonequilibrium boundary conditions for the latter we soon discovered, in retrospect and to our surprise, that all the nonequilibrium motion equations we had fashioned were time-reversible, so that any short trajectory fragment, advancing from one time to another, could be precisely reversed. One could do so by changing the signs of the momenta as well as all of the time-reversible friction coefficients (described in the next Section) used to impose thermal boundary conditions on the simulations. The most surprising consequence of the simulations, that irreversible behavior was generated by time-reversible equations of motion, fascinated us just as it had Boltzmann a century earlier. In the next Section we explore examples of time reversibility with two models, one of them with the desirable property of “ergodicity” and the other one not.

III. NONEQUILIBRIA, TIME REVERSIBILITY, AND ERGODICITY

A. Nonequilibrium Thermostatted Systems

Following my six years’ experience working with Francis on virial series (density expansions of the pressure), and equation of state problems I was convinced that equilibrium statistical mechanics and corresponding computer simulations were understood sufficiently well. I set out to study nonequilibrium systems driven by differences in velocity or temperature. Invariably I sought out the simplest possible systems for detailed studies. According to kinetic theory diffusion can be studied by following a single moving particle through an array of scatterers. Simulating viscous flow requires at least two oppositely-moving particles,

and heat flow three, or so I thought then.

Some 30 years later, in 1997, Harald Posch and I formulated two new *single-particle* models for thermostatted heat conductivity⁷. In both these cases we studied the motion of a single nonequilibrium oscillator exposed to a smoothly-varying temperature gradient (dT/dq) with a maximum value of ϵ :

$$T(q) \equiv 1 + \epsilon \tanh(q) \rightarrow \{ 1 - \epsilon < T < 1 + \epsilon ; | (dT/dq) | \leq \epsilon \} .$$

This coordinate-dependent temperature $T(q)$ was controlled with either a single Nosé-Hoover⁸ “thermostat” variable ζ :

$$\{ \dot{q} = p ; \dot{p} = -q - \zeta p ; \dot{\zeta} = p^2 - T(q) \} [\text{NH}] ,$$

or, following my 1996 work with Brad Holian⁹, with two such control variables, ζ and ξ :

$$\{ \dot{q} = p ; \dot{p} = -q - \zeta p - \xi p^3 ; \dot{\zeta} = p^2 - T(q) ; \dot{\xi} = p^4 - 3p^2 \} [\text{HH} = \text{PH}] .$$

Here the time-reversible controls, ζ and ξ , provided the initial conditions allow it, drive a purely-kinetic heat current ($p^3/2$) and generate a nonequilibrium steady state in three-dimensional (q, p, ζ) or four-dimensional (q, p, ζ, ξ) phase space. The steady state is the time-averaged probability density in the phase space. In the “equilibrium” case, where temperature is constant, $T = 1$, the time-averaged second and fourth moments are constrained by ζ and ξ to the values from Gibbs’ canonical ensemble with $T \equiv 1$, $\langle p^2, p^4 \rangle = 1, 3$.

The three- and four-dimensional descriptions of a nonequilibrium oscillator turned out quite differently to the predictions of Gibbs’ ensembles. Nonequilibrium distributions are typically “fractal” and can be quite intricate far from equilibrium. **Figure 1** compares a two-dimensional (q, p) phase-space cross section cut through a four-dimensional representation of HH=PH dynamics to the corresponding cross section using HH=SHH dynamics.

In both cases the imposed temperature varies in space, $T(q) \equiv 1 + 0.4 \tanh(q)$. In my more recent 2014 work with Clint Sprott¹⁰ and my Wife Carol we used a more-elaborate motion equation for the quartic control variable ξ :

$$\{ \dot{q} = p ; \dot{p} = -q - \zeta p - \xi p^3 ; \dot{\zeta} = p^2 - T(q) ; \dot{\xi} = p^4 - 3p^2 T(q) \} [\text{HH} = \text{SHH}] .$$

The comparison of the two fractal cross sections given in **Figure 1** shows that the two similar $\dot{\xi}$ control equations produce very different fractals far from equilibrium.

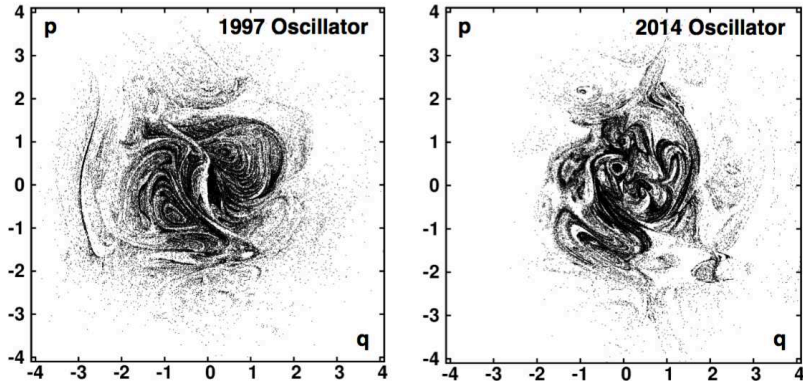


FIG. 1: $p(q)$ sections with $\zeta = \xi = 0$ for two versions of a conducting oscillator with both quadratic and quartic moments controlled by the PH and SHH generalizations of the Hoover-Holian motion equations given in the text. Here the maximum temperature gradient ϵ is 0.40.

B. Time Reversibility, Dissipation, and the Second Law of Thermodynamics

Notice that both the Nosé-Hoover and the Hoover-Holian sets of motion equations *are* “time-reversible”. By this I mean that changing the signs of the time, the momentum p , and the friction coefficients ζ and ξ precisely reverses the time-development of the coordinate q . An undesirable feature of the simpler Nosé-Hoover thermostat model is that it often lacks ergodicity^{8,10} when applied to small systems. In the conducting oscillator example problem the three-dimensional (q, p, ζ) phase space contains infinitely-many stationary states, mostly two-dimensional tori with no nonequilibrium heat flux. This disturbing abundance of unphysical solutions can be cured by introducing the additional control variable ξ which originated in the Hoover-Holian example⁹.

With ξ included, the resulting phase-space distributions are typically fractal (fractional-dimensional) attractors, as suggested by the two sample cross-sections of **Figure 1**. In such fractals the distribution of time-reversible (q, p, ζ, ξ) states describes an irreversible dissipative flow of kinetic energy *from* a mirror-image repeller *to* its attractor. The resulting hot-to-cold direction of the mean energy flow is just that mandated by the macroscopic Second Law of Thermodynamics. Though the additional control variable ξ increases the dimensionality of phase space from three to four this extra complexity seems a reasonable price to pay for the simplicity of ergodicity.

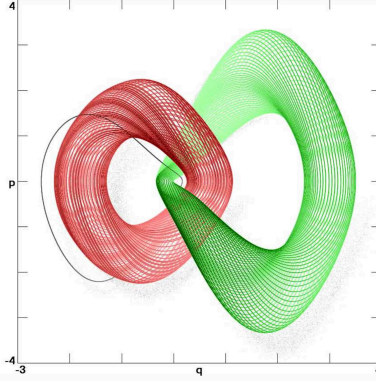


FIG. 2: Three disconnected solutions for the Nosé-Hoover oscillator with $\epsilon = 0.42$. The red and green toroidal solutions and the black dissipative limit cycle all satisfy exactly the same nonequilibrium motion equations, with $T(q) = 1 + \epsilon \tanh(q)$.

C. Ergodicity and Ergodic Nonequilibrium Fractals

At equilibrium ergodicity is crucial for the validity of Willard Gibbs’ statistical mechanics. Gibbs was able to formulate macroscopic thermodynamic properties as microscopic phase-space averages provided that all the phase-space states included in the averages were accessible dynamically, one from another. An “ergodic” system is one in which the phase-space average is equivalent to a longtime dynamical average. Evidently the thermostatted Nosé-Hoover oscillator just considered is not ergodic – each of the three solutions of **Figure 2** is confined to its own one- or two-dimensional portion of the three-dimensional (q, p, ζ) space. In striking contrast the two similar Hoover-Holian oscillators of **Figure 1** used two friction coefficients and provided ergodic nonequilibrium steady states independent of initial conditions⁸⁻¹⁰.

The fractal nature of nonequilibrium flows is typical of ergodic stationary states^{11,12}. Such fractals are invariably chaotic and anisotropic, with an overall positive Lyapunov exponent describing the mean (time-averaged) separation rate of two nearby phase-space trajectories. Additionally, one or more negative exponents cause the overall negative sum responsible for the zero-phase-volume steady-state structures of fractal phase-space attractors: $d \ln(\otimes)/dt \equiv \sum \lambda_i < 0$. Here \otimes is an infinitesimal element of comoving phase-space volume. Because the summed-up Lyapunov exponents on the repeller (with their opposite signs) are positive rather than negative any nearby trajectory undergoes an exponentially-fast departure from the well-named repeller to the dissipative strange attractor. The typical case, in which

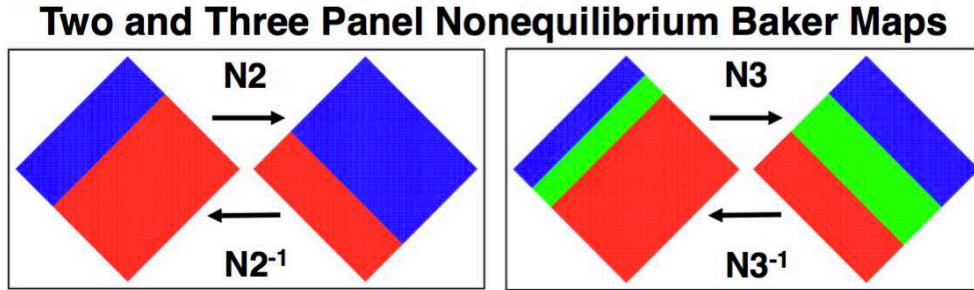


FIG. 3: Tricolor representations of the N2 and N3 maps. In both cases the rectangular areas prior to mapping are deformed without rotation, shrinking and expanding in orthogonal directions. Iterations of these linear maps and their inverses provide fractal structures resembling those generated with nonlinear dissipative flows. See Figure 4.

both structures have a presence throughout the phase space, renders the mental picture of repeller-to-attractor flow somewhat paradoxical.

By 1987 it became clear that phase-space distributions for nonequilibrium stationary states were typically fractal and ergodic in character^{11,12} with a wide assortment of fractional dimensions which were defined and described by Rényi, Mandelbrot, and a huge literature of follow-on work. Harald Posch and I found that two-dimensional maps, clearly simpler than three- and four-dimensional flows, could be chosen to model the properties of time-reversible nonequilibrium simulations¹³. We chose to study the compressible time-reversible Baker Map shown at the left of **Figure 3**. Iterating the map converts one (q, p) state to another and another and another \dots , rather like the sequence of discrete movie frames used to describe a continuous motion. Extensions of this work¹⁴, some very recent^{15,16}, have confronted us with some surprising and stimulating results. I describe those next.

IV. MAPS CARICATURING NONEQUILIBRIUM STATISTICAL FLOWS

Time-reversible molecular dynamics can be applied equally well to equilibrium systems and to nonequilibrium atomistic flows of mass, momentum, and energy. Despite reversibility the motion equations used to model steady flows invariably produce dissipative irreversibility, as is required by the Second Law of Thermodynamics^{11,12}. One can best seek to grasp an understanding of how reversible equations provide irreversible behavior by the study of small systems well suited to support using computer graphics. Such investigations revealed that the mechanism for computational irreversibility is a consequence of the fractal repeller-to-

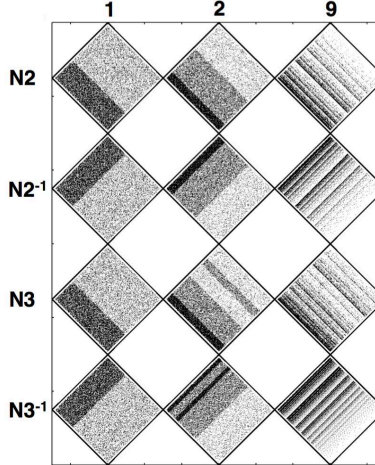


FIG. 4: Results obtained by iterating N2 and N3 and their inverses once, twice, and nine times. Notice that the iterations for N2 forward and backward are mirror images due to the time-reversibility of those maps. The lack of this symmetry for iterations of N3 and $N3^{-1}$ shows that those more complex maps lack time-reversibility.

attractor nature of time-reversible nonequilibrium phase-space states.

I turn here from flows to maps, stressing recent results. This choice simplifies and clarifies analyses. Like flows, maps are deterministic, can be time-reversible, and often generate fractals. Their phase-space compressibility rate, $(d \ln \otimes / dt) = \sum \lambda_i$, is closely related to the Gibbs-entropy production rate $\dot{S} = k \ln \dot{\otimes}$ and to the fractal information dimension, just as is the case with flows. Here \otimes is an infinitesimal element of phase volume comoving with the flow and k is Boltzmann's constant.

There is one interesting qualitative difference between flows and maps: irreversibility in flows stems from nonlinearity while even the simplest linear maps can illustrate the dissipative behavior obeying the Second Law. Let us next compare the compressible but time-reversible linear Baker Map of 30 years ago to a similar one which lacks time reversibility but retains the dissipative fractal character of typical nonequilibrium flows.

V. OF TWO LINEAR BAKER MAPS, N2 IS REVERSIBLE WHILE N3 IS NOT

Two-Dimensional Maps are analogous to cross-sections of Three-Dimensional Flows. Here we consider the interesting fractal structures generated by two similar simple linear maps, N2 and N3, which operate within the finite diamond-shaped domains shown in **Figures 3 and 4**.

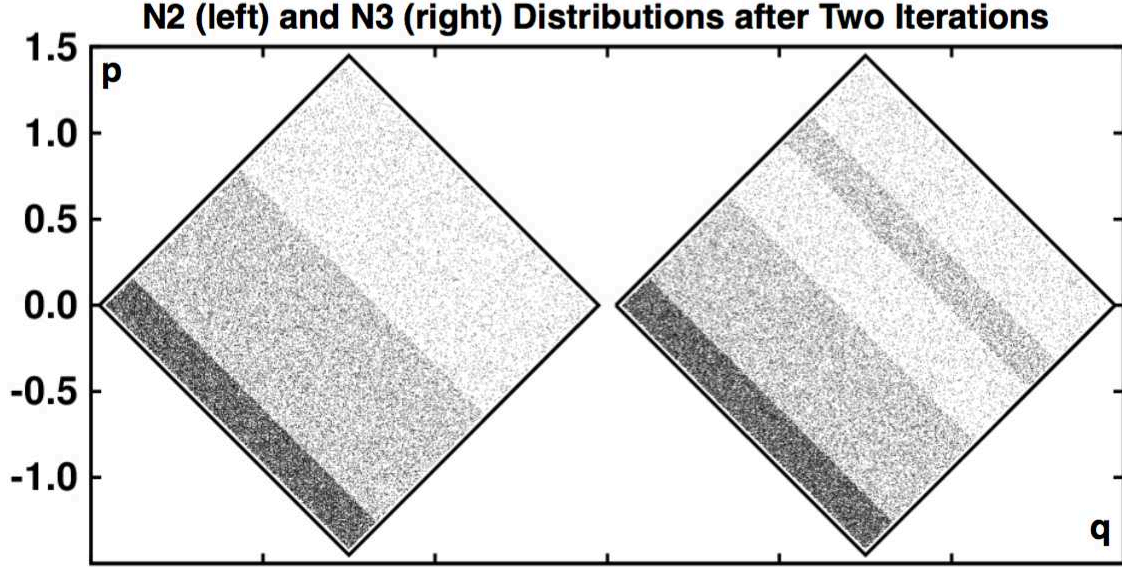


FIG. 5: The distributions of 50,000 random initial points after two forward mappings of N2 and N3. The three different densities of points, relative to a unit square, are 4, 1, and $1/4$, giving identical information dimensions for the two distributions shown here.

The reason for the diamond-shaped (q, p) domains chosen here is linked to time reversibility. Time Reversibility is a stringent constraint on maps. It requires that the “before” and “after” regions have identical shapes and sizes. This requirement is easily satisfied with N2 where there is a single discontinuity in the mapping between two rectangles with different areas. Here time reversibility is easy to check. We adopt the conventional three-step meaning: the effect of the mapping can be reversed to reach the previous condition, by carrying out three successive steps, $T*N2*T$. These correspond to [1] time-reversal, [2] forward mapping, and [3] a second time reversal. Here T is the time-reversal map $[T(\pm q, \pm p) = (\pm q, \mp p)]$, changing the sign of the momentum p but leaving the coordinate q unchanged.

Baker Maps take a point in two-dimensional (q, p) [coordinate, momentum] space from one iteration to the next. Such a mapping can be applied to individual points or to areas in two-dimensional (q, p) phase space. Two similar linear Baker Maps, along with their inverses confined to the same portion of two-dimensional space, are illustrated in **Figures 3-7**. I have written the analytic forms of all the maps so that they occupy diamond-shaped domains with maximum and minimum values of the horizontal coordinate q and the vertical momentum p equal to $\pm\sqrt{2}$ so that the map area is 4 and the diamonds’ centers are at the origin.

In describing the density within these diamonds it is convenient to imagine them mapped to a unit square with the density integrated over the square equal to unity. In speaking of the density in discussing Figures 5 and 9 and 10 we will adopt the picture that the probability density occupies a unit square and that the total density integrates to unity.

In the (q, p) coordinate system appropriate to diamond domains the analytic forms of the simplest time-reversible N2 map and its inverse are as follows :

```

if(q-p.lt.-4*d) qnew = + (11/ 6)*q - ( 7/ 6)*p + 14*d
if(q-p.lt.-4*d) pnew = - ( 7/ 6)*q + (11/ 6)*p - 10*d
if(q-p.ge.-4*d) qnew = + (11/12)*q - ( 7/12)*p - 7*d
if(q-p.ge.-4*d) pnew = - ( 7/12)*q + (11/12)*p - 1*d
[ Reversible Nonequilibrium Baker Map N2 with d = sqrt(1/72) ]

```

The inverse mapping $N2^{-1}$ follows easily from the linear equations, with the result :

```

if(q+p.lt.-4*d) qnew = + (11/ 6)*q + ( 7/ 6)*p + 14*d
if(q+p.lt.-4*d) pnew = + ( 7/ 6)*q + (11/ 6)*p + 10*d
if(q+p.ge.-4*d) qnew = + (11/12)*q + ( 7/12)*p - 7*d
if(q+p.ge.-4*d) pnew = + ( 7/12)*q + (11/12)*p + 1*d
[Inverse of the Nonequilibrium Baker Map N2 ]

```

The time-reversibility of the N2 map guarantees that the inverse mapping is equivalent to the three-step process mentioned above, $T*N2*T$. For flows this reversal analog for a timestep $+dt$ corresponds to taking a *negative* timestep $-dt$ and then changing the sign of the momentum. Because all the maps we consider here are Lyapunov unstable (more about this later) the practical length of a reversed trajectory is limited by the exponential growth of roundoff error. With quadruple-precision arithmetic a typical sequence of N2 or N3 mappings can be recognizably reversed for about fifty iterations.

The N2 and N3 mappings of **Figures 3-7** are similar, but differ in one fundamental way. The N3 mapping is *not reversible*, though Carol and I mistakenly thought that it was¹⁵. The inverse mapping follows easily from the linear equations just as in the N2 case. But the inverse is not at all the same as the three-step mapping $T*N*T$ which applies in the time-reversible case.

```

if (q-p.lt.-8*d)          qnew = +19*q/ 6 - 17*p/ 6 + 34*d
if (q-p.lt.-8*d)          pnew = -17*q/ 6 + 19*p/ 6 - 26*d
if((q-p.ge.-8*d).and.(q-p.le.-4*d)) qnew = +19*q/ 6 - 17*p/ 6 + 18*d
if((q-p.ge.-8*d).and.(q-p.le.-4*d)) pnew = -17*q/ 6 + 19*p/ 6 - 18*d
if (q-p.gt.-4*d)          qnew = +11*q/12 - 7*p/12 - 7*d
if (q-p.gt.-4*d)          pnew = - 7*q/12 + 11*p/12 - 1*d
[ Irreversible Nonequilibrium Baker Map N3 with d = sqrt(1/72) ]

if (q+p.ge.+4*d)          qnew = +19*q/12 + 17*p/12 - 17*d
if (q+p.ge.+4*d)          pnew = +17*q/12 + 19*p/12 - 7*d
if((q+p.lt.+4*d).and.(q+p.gt.-4*d)) qnew = +19*q/12 + 17*p/12 - 3*d
if((q+p.lt.+4*d).and.(q+p.gt.-4*d)) pnew = +17*q/12 + 19*p/12 + 3*d
if (q+p.le.-4*d)          qnew = +11*q/ 6 + 7*p/ 6 + 14*d
if (q+p.le.-4*d)          pnew = + 7*q/ 6 + 11*p/ 6 + 10*d
[ Inverse of the Nonequilibrium Baker Map N3 ]

```

Figures 4-7 show the evolution of the fractals, comparing the forward and backward developments for N2, N3, and their inverses. **Figure 4** compares the distributions after one, two, and nine forward mappings. The detailed structures of the limiting attractors for all four maps are shown in **Figures 6 and 7**. Notice particularly that the N3 attractor and repeller are quite different fractals, not mirror images of one another and with different fractal dimensions. This is confirmation that N3 and its inverse are not time-reversible.

VI. THE IRREVERSIBLE N3 MAP AND ITS INFORMATION DIMENSION

The N3 map was motivated by the idea to symmetrize the “after” image of the N2 map shown in **Figure 3** to provide the three equal-area regions shown at the right of the Figure. Although the linear equations describing the N3 map and its inverse are readily constructed and given above, we can see that the attractor and repeller shown in **Figure 7** are not mirror images. They are particularly simple from a structural point of view. It is easy to verify that T^*N3^*T , where T reverses the sign of the vertical (momentum) coordinate p , does not result in the inverse $N3^{-1}$.

Consider the action of N3 on a uniform distribution. The first iteration results in three

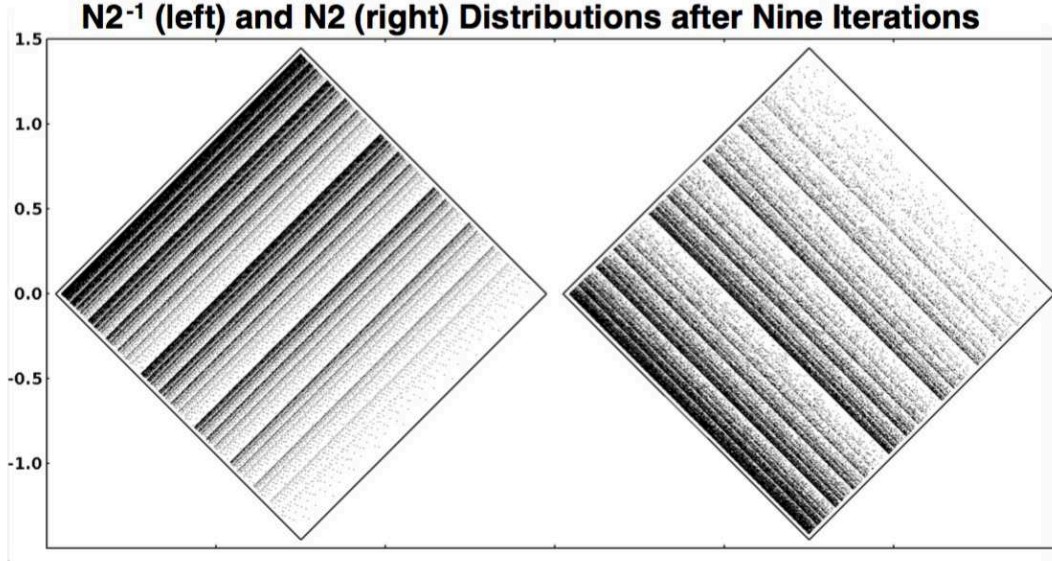


FIG. 6: Repellor (left) and Attractor (right) for N2, corresponding to nine iterations, visually quite similar to the limiting infinite-iterations case. 200,000 points are shown. The repellor/attractor pair are mirror images of each other where the mirror is horizontal.

strips of equal width (red, green, and blue at the right of **Figure 3**), with densities $\{2, \frac{1}{2}, \frac{1}{2}\}$ and probabilities $\{\frac{2}{3}, \frac{1}{6}, \frac{1}{6}\}$. The corresponding information dimension is :

$$D_I = 1 + [\frac{2}{3} \ln \frac{2}{3} + \frac{1}{3} \ln \frac{1}{6}] / \ln \frac{1}{3} = 1.78969 .$$

A second iteration (third row and second column of **Figure 4** provides nine strips of width $\frac{1}{9}$, with densities $\{4, 1, 1, 1, \frac{1}{4}, \frac{1}{4}, 1, \frac{1}{4}, \frac{1}{4}\}$, giving for the information dimension :

$$D_I = 1 + [\frac{4}{9} \ln \frac{4}{9} + \frac{4}{9} \ln \frac{1}{9} + \frac{1}{9} \ln \frac{1}{36}] / \ln \frac{1}{9} = 1.78969 .$$

Continuing the iteration of the map produces no change, just repetition of the result $D_I(N3) = 1.78969$.

N2 on the other hand provides a different distribution of densities, but only different in their ordering : $\{4, 1, 1, 1, 1, \frac{1}{4}, \frac{1}{4}, \frac{1}{4}, \frac{1}{4}\}$. **Figure 5** compares the distributions according to N2 and N3 after just two iterations of the mapping, starting with a uniform distribution. The three different densities of points shown in the distributions differ from each other by powers of 4, as illustrated explicitly above. Evidently, by construction, the information dimensions for the two maps are identical, equal to 1.78969. In the next Section we will see that this is false!

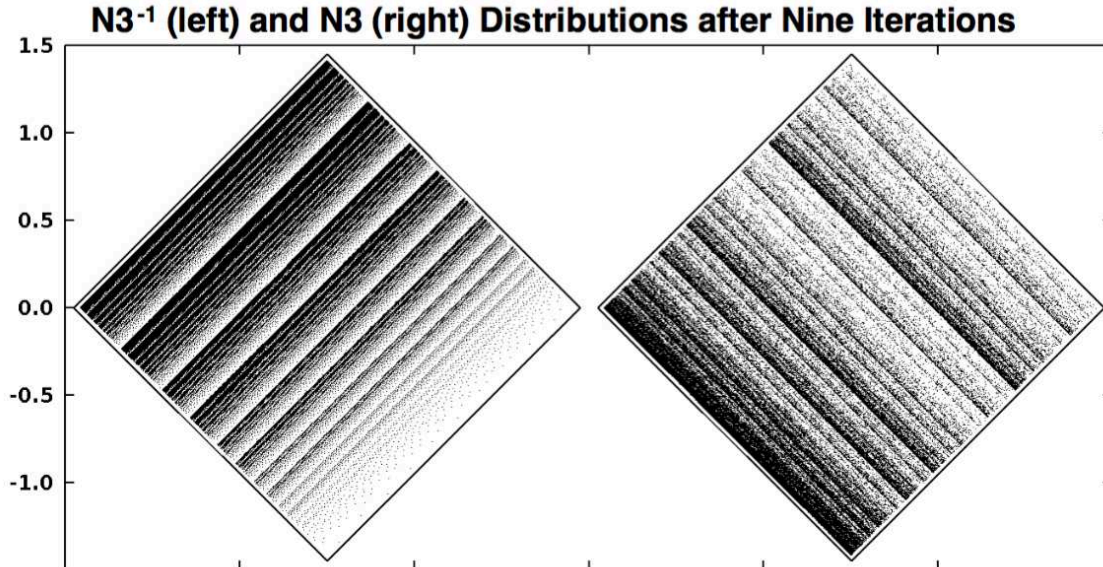


FIG. 7: Repellor (left) and Attractor (right) for N3. Notice that time-reversibility symmetry is absent. The repellor generated by $N3^{-1}$ is also fractal, but with a different information dimension than that of the attractor, and with a much steeper falloff of density, as shown in Figure 9.

VII. SYMMETRY OF THE REPELLOR AND ATTRACTOR

Although the attractors of the N2 and N3 maps appear to have the same information dimensions, as quantified above, numerical work tells a different story, and in an interesting way, illustrated in **Figure 8**. There we choose a particular mesh, $3^{-5} = \frac{1}{243}$, and compute the information dimension after each of several iterations. Nine, as well as the limiting value, are shown in the figure. Through the fifth iteration the information dimensions for N2 and N3 agree precisely. After that iteration the dimension of the N3 map remains unchanged at 1.78969 while that of N2 continues to fall, as shown in **Figure 8**. Careful numerical work on the N2 problem^{16,17} has suggested two different values (!) for the information dimension of N2, neither of them equal to 1.78969: 1.7337 and 1.741₅. The first of these is the Kaplan-Yorke estimate,

$$D_{KY} = 1 - (\lambda_1/\lambda_2) .$$

where the Lyapunov exponents $\lambda_1 > 0$ and $\lambda_2 < 0$ are evaluated in the following Section. The second estimate $D_I \stackrel{?}{=} 1.741_5$ is the result of trillion-iteration simulations of the N2 mapping using meshes that are integral powers of (1/3) as high as 3^{-20} . The resolution of this uncertainty has been set as the 2020 Snook Prize problem¹⁵.

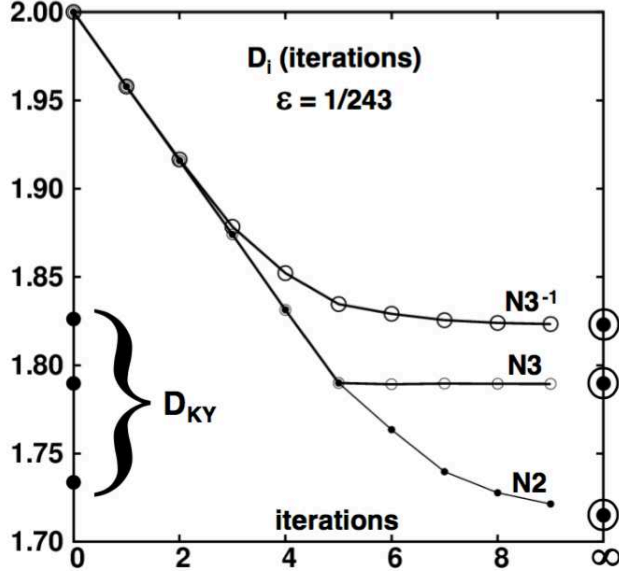


FIG. 8: Information dimensions for N2, N3, and N3⁻¹ using 243 mesh points as functions of the number of map iterations. D_I remains the same for N2 and N3 through five iterations, but their limiting information dimensions (circled) differ. Further mesh refinements extend the agreement but in the end the convergence remains nonuniform. The Kaplan-Yorke conjectured dimensions are shown at the left and suggest that N3 and its inverse obey that conjecture while N2 may not.

VIII. LYAPUNOV INSTABILITY OF COMPRESSIBLE MAPS

The Lyapunov exponents of maps, like those of flows, describe the rate at which two nearby points separate. The N2 map gives threefold expansion with orthogonal $\frac{3}{2}$ -fold compression one third of the time (see the blue panel at the left of **Figure 3** and $\frac{3}{2}$ -fold expansion with orthogonal threefold compression two-thirds of the time (the red panel), corresponding to the Lyapunov exponents:

$$\lambda_1 = \frac{1}{3} \ln(3) + \frac{2}{3} \ln \frac{3}{2} = \frac{1}{3} \ln \frac{27}{4} = +0.636514 ;$$

$$\lambda_2 = \frac{1}{3} \ln \frac{2}{3} + \frac{2}{3} \ln \frac{1}{3} = \frac{1}{3} \ln \frac{2}{27} = -0.867563 .$$

The N3 map can be analyzed similarly following **Figure 3**, with the results

$$\lambda_1 = \frac{1}{3} \ln(6) + \frac{2}{3} \ln \frac{3}{2} = \frac{1}{3} \ln \frac{27}{2} = 0.867563 ;$$

$$\lambda_2 = \frac{1}{3} \ln \frac{1}{3} + \frac{2}{3} \ln \frac{1}{3} = \frac{1}{3} \ln \frac{1}{27} = -1.098612 .$$

These results are of interest in view of the Kaplan-Yorke conjecture that the fractal dimension for such a map is given by $D_{KY} = 1 - (\lambda_1/\lambda_2)$, 1.73368 for N2 and 1.78969 for N3. Thus the

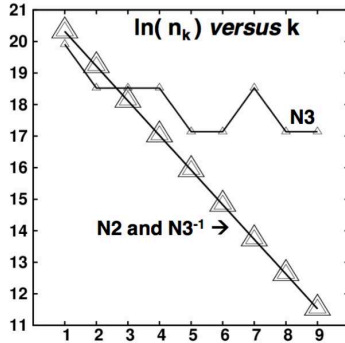


FIG. 9: Occupants of panels of width $(1/3)$, $(2/9)$, $(4/27)$, \dots , or $(1/3)(2/3)^{k-1}$ with panel indices $1 \leq k \leq 9$. Each point is taken from a sampling of one billion iterations. Both N2 and N3⁻¹ have the same “unit-square-based” panel densities of $(1/2)^{k-2}$. The N3 mapping here, for nine panels of equal width, produces densities varying as powers of 4.

unchanging information dimension for the N3 map with increasing iterations agrees precisely with the Kaplan-Yorke conjecture while that of the somewhat simpler N2 map does not.

IX. ITERATION OF THE MAPS GIVES FRACTAL ATTRACTORS

The two maps give similar strange attractors. We saw that N3 has the more “conventional” behavior, relative to N2, in that the information dimension after a single iteration [applied to a constant density throughout the diamond-shaped domain] is the same as that for many iterations and is also equal to the information dimension which follows from the Kaplan-Yorke conjecture

$$D_I \stackrel{?}{=} D_{KY} = 1 - (\lambda_1/\lambda_2) = 1.789690 .$$

Figures 6 and 7 show the attractors and repellers for the two maps. The N2 map shows the expected symmetry for time-reversible maps. The repeller and attractor are mirror images of each other. The N3 map is different though its repeller is “simpler” than the N2 fractals. The data in **Figure 8** indicate that N3 and its inverse have different information dimensions. In fact the differences are qualitative. A look at **Figure 7** correctly suggests that the fractal generated by N3 consists of three similar panels. The density pattern in the southwest third of the figure is repeated, with a density four times lower, in the middle and northeast thirds of the domain. On the other hand the attractor of the inverse map N3⁻¹

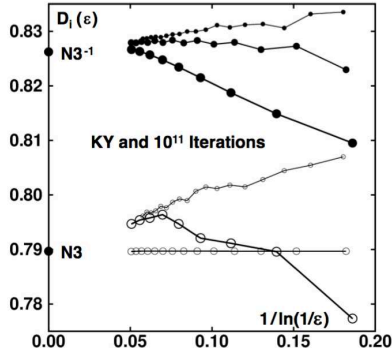


FIG. 10: Mesh-dependent information dimension estimates for the $N3$ and $N3^{-1}$ map with meshes varying from $(1/2)^8$ to $(1/2)^{25}$ (fine lines), $(1/3)^5$ to $(1/3)^{18}$ (medium lines), and $(1/6)^3$ to $(1/6)^{11}$ (thick lines). The rapid convergence of the $N3$ map data with meshes of $(1/3)^n$ is promoted by its threefold symmetry, as shown in Figs. 3 and 7.

repeats its northwest third (with two-thirds the density) infinitely-many times toward the southeast in panels of widths of $(1/2)(2/3)^k$ with overall densities 2^{2-k} for all positive k . The $N2$ map and its inverse behave in exactly this same way, with two thirds of their points in the densest third of the diamond, giving densities of 2^{2-k} for all positive k . **Figure 9** illustrates these fractal dependencies with a sampling of a billion, $e^{20.723}$, points.

Figure 10 shows the convergence of finite-mesh samplings of 10^{11} iterations, binned into meshes as small as $(1/2)^{25}$, $(1/3)^{18}$, and $(1/6)^{11}$. These data indicate that both $N3$ and its inverse $N3^{-1}$ satisfy the Kaplan-Yorke conjecture where the Kaplan-Yorke values are shown as the zero-mesh limits. Meanwhile the data for $N2$ are confusing. An explanation or clarification of this confusion is the subject of the 2020 Snook Prize¹⁸.

X. SUMMARY

The small-system explorations begun with Francis Ree, emphasizing simple models well-suited to computer simulation, have provided the details of the melting and freezing transitions for hard particles as well as the connection of thermostatted nonequilibrium simulations to the Second Law of Thermodynamics and Irreversibility. The finding of fractal phase-space structures led to the investigation of maps, whose history goes back to Hopf's work in 1937. The maps, though simpler than flows, have very recently led to findings that are a surprise, suggesting that there is more to learn about the fractal structures that play an important role in statistical mechanics.

XI. JOINT PUBLICATIONS OF FRANCIS REE AND THE AUTHOR

We published nine joint works, all of them in the Journal of Chemical Physics, including one written jointly with Berni Alder. The volume numbers are indicated in this list: Fifth and Sixth Virial Coefficients for Hard Spheres and Hard Disks **40**; On the Signs of the Hard Sphere Virial Coefficients **40**; Reformulation of the Virial Series for Classical Fluids **41**; Dependence of Lattice Gas Properties on Mesh Size **41** [with Berni Alder]; Calculation of Virial Coefficients. Squares and Cubes with Attractive Forces **43**; Thermodynamic Properties of a Simple Hard-Core System **45**; Seventh Virial Coefficients for Hard Spheres and Hard Disks **46**; Use of Computer Experiments to Locate the Melting Transition and Calculate the Entropy in the Solid Phase **47**; Melting Transition and Communal Entropy for Hard Spheres **49**.

-
- ¹ B. J. Alder and T. E. Wainwright, “Molecular Motions”, *Scientific American* **201**, 113-126 (1959).
 - ² W. G. Hoover and A. G. De Rocco, “Sixth and Seventh Virial Coefficients for the Parallel Hard-Cube Model”, *Journal of Chemical Physics* **36**, 3141-3162 (1962).
 - ³ A. G. De Rocco and W. G. Hoover, “Second Virial Coefficient for the Spherical Shell Potential”, *Journal of Chemical Physics*, **36**, 916-926 (1962).
 - ⁴ F. H. Ree, T. S. Ree, T. Ree, and H. Eyring, “Random Walk and Related Physical Problems”, in *Advances in Chemical Physics* **4**, 1-66 (1962), edited by I. Prigogine.
 - ⁵ A list of 161 of Francis Ree’s publications can be found (in January 2020) on the ResearchGate website. Francis’ LLNL obituary can be found at “<https://www.llnl.gov/community/retiree-and-employee-resources/in-memoriam/francis-ree>”.
 - ⁶ W. G. Hoover and W. T. Ashurst, “Nonequilibrium Molecular Dynamics”, in *Theoretical Chemistry* **1**, 1-51 (Academic, New York, 1975).
 - ⁷ H. A. Posch and W. G. Hoover, “Time-Reversible Dissipative Attractors in Three and Four Phase-Space Dimensions”, *Physical Review E* **55**, 6803-6810 (1997).
 - ⁸ W. G. Hoover, “Canonical Dynamics: Equilibrium Phase-Space Distributions”, *Physical Review A*, **31**, 1695-1697 (1985).

- ⁹ W. G. Hoover and B. L. Holian, “Kinetic Moments Method for the Canonical Ensemble Distribution”, *Physics Letters A* **211**, 253-257 (1996).
- ¹⁰ J. C. Sprott, W. G. Hoover, and C. G. Hoover, “Heat Conduction, and the Lack Thereof, in Time-Reversible Dynamical Systems: Generalized Nosé-Hoover Oscillators with a Temperature Gradient”, *Physical Review E* **89**, 042914 (2014).
- ¹¹ B. L. Holian, W. G. Hoover, and H. A. Posch, “Resolution of Loschmidt’s Paradox: The Origin of Irreversible Behaviour in Reversible Atomistic Dynamics”, *Physical Review Letters* **59**, 10-13 (1987).
- ¹² W. G. Hoover, H. A. Posch, B. L. Holian, M. J. Gillan, M. Mareschal, and C. Massobrio, “Dissipative Irreversibility from Nosé’s Reversible Mechanics”, *Molecular Simulation* **1**, 79-86 (1987).
- ¹³ Wm. G. Hoover and H. A. Posch, “Chaos and Irreversibility in Simple Model Systems”, *Chaos* **8**, 366-373 (1998).
- ¹⁴ J. Kumičák, “Irreversibility in a Simple Reversible Model”, *Physical Review E* **71**, 016115 (2005).
- ¹⁵ W. G. Hoover and C. G. Hoover, “Aspects of Dynamical Simulations, Emphasizing Nosé and Nosé-Hoover Dynamics and the Compressible Baker Map”, *Computational Methods in Science and Technology* **25**, 125-141 (2019).
- ¹⁶ W. G. Hoover and C. G. Hoover, “Molecular Dynamics, Fractal Phase-Space Distributions, the Cantor Set, and Puzzles Involving Information Dimensions for Two Compressible Baker Maps”, *Regular and Chaotic Dynamics* (submitted January 2020) = arXiv 2001.02541.
- ¹⁷ W. G. Hoover and C. G. Hoover, “Random Walk Equivalence to the Compressible Baker Map and the Kaplan-Yorke Approximation to Its Information Dimension”, arXiv:1909.04526 (2019).
- ¹⁸ W. G. Hoover and C. G. Hoover, “2020 Ian Snook Prize Problem: Three Routes to the Information Dimensions for One-dimensional Stochastic Random Walks and Their Equivalent Two-Dimensional Baker Maps”, *Computational Methods in Science and Technology* **25**, 153-159 (2019).